

B 6 Structure and phase behavior of polymer systems

Marcus Müller

Institut für Theoretische Physik

37077 Göttingen Germany

Contents

| | | |
|----------|--|-----------|
| 1 | Coarse-grained polymer models | 2 |
| 2 | Model and techniques | 3 |
| 2.1 | Computer simulations | 3 |
| 2.2 | Self-consistent field (SCF) theory | 6 |
| 2.2.1 | “Single-chain-in-mean-field”-simulations | 8 |
| 2.3 | Applications | 10 |
| 2.4 | Phase behavior of homopolymer blends | 10 |
| 2.5 | Interfacial properties | 15 |
| 2.6 | Self-assembly of diblock copolymers | 19 |
| 3 | Outlook | 24 |

1 Coarse-grained polymer models

Polymeric materials are ubiquitous [1] – applications range from common things like windows frames, plastic cups, or insulation materials to nanoscopically structured materials for filtration, catalysis or microelectronic devices. Polymers are long string-like macromolecules that adopt random walk-like conformations in a dense melt. Much of the qualitative behavior of dense multi-component polymer systems can be understood from a coarse-grained description. The large spatial extension of the macromolecules imparts a great deal of universality on their behavior: (i) the characteristic length scale is set by the extension of the molecule, as measured by the mean-square end-to-end distance, R_e^2 , and (ii) one molecule interacts with many neighbors. The former property implies that details of the atomistic scale influence the behavior on the scale of the entire molecule (and larger) only via a small number of coarse-grained parameters that encode the microscopic structure. The latter property implies that long-wavelength fluctuations are strongly suppressed and that the behavior on large length scales is rather well describable by mean field theories. Let N be the number of segments along the backbone of a polymer molecule and ρ denote the segment number density of the dense solution or melt, then there are on the order of $\sqrt{\bar{N}} \equiv \rho R_e^3 / N$ other molecules inside of the volume of a reference chain. \bar{N} characterizes the degree of interdigitation of the molecules and in the limit $\bar{N} \rightarrow \infty$ long wave length fluctuations are suppressed. In a melt the chain conformations are random walk-like – $R_e^2 = b^2 N$ (b being the statistical segment length) – such that $\bar{N} = (\rho b^3)^2 N$ is proportional to the number of segments. Since \bar{N} is independent from the way how we define a segment, it is called the invariant degree of polymerization. R_e and \bar{N} are the two coarse-grained parameters that encode the microscopic chemical structure of a one-component polymer melt.

In the following we consider binary polymer systems that consist of two different types of segments – A and B . Different segments repel each other and the strength of the repulsive interaction of segments measured in units of $k_B T$ is set by the Flory-Huggins parameter, χ . In the case of a binary polymer blend, where both species are comprised of the same number of segments, N the excess free energy of mixing (per segment) has the form of a regular solution [2]:

$$\Delta F(\varphi_A) = k_B T \frac{\rho \varphi_A}{N} \ln \rho \varphi_A + k_B T \frac{\rho \varphi_B}{B} \ln \rho \varphi_B + k_B T \rho \chi \varphi_A \varphi_B \quad (1)$$

where $0 \leq \varphi_A = 1 - \varphi_B \leq 1$ denotes the composition of the incompressible mixture. The first term is the entropy of mixing (or translational entropy) which is reduced by a factor N due to the chain connectivity. The last term denotes the excess energy of mixing. Since the entropy of mixing is very small for long chain molecules different polymers tend to phase separate. Of course, the free energy per segment explicitly depends on the definition of a segment and it is convenient to rewrite it in terms of the invariant, coarse-grained parameters, \bar{N} and χN :

$$\frac{\Delta F(\varphi_A)}{k_B T} = \sqrt{\bar{N}} (\varphi_A \ln \varphi_A + \varphi_B \ln \varphi_B + \chi N \varphi_A \varphi_B) \quad (2)$$

In this contribution I will discuss computer simulation and mean field techniques to describe dense multicomponent polymer systems. In the next section coarse-grained models are introduced and numerical techniques to study their structure and thermodynamic behavior are discussed. In the subsequent section these techniques are illustrated by a few selected applications for binary homopolymer blends and the self-assembly of lamellar forming diblock copolymers. The contribution concludes with a brief outlook.

2 Model and techniques

2.1 Computer simulations

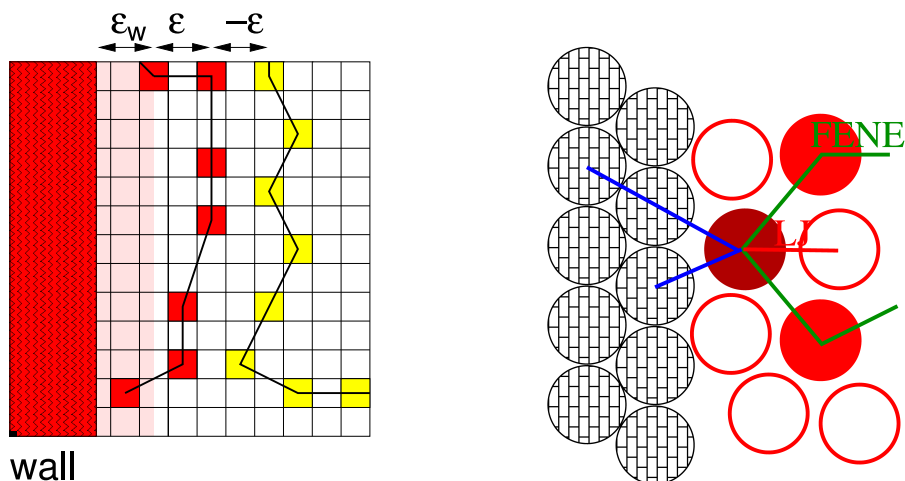


Fig. 1: (a) Illustration of the bond fluctuation model [3]. (b) Sketch of a bead-spring off-lattice model. See text for explanations.

Computer simulations of coarse-grained, particle-based models numerically investigate the structure and thermodynamics of a model polymer system without any approximation. Coarse-grained, particle-based models represent linear macromolecules as a string of bonded segments interacting via potentials of finite range. They must include three relevant properties to capture the universal behavior of dense multi-component systems of large length scales: connectivity of segments along the backbone of the molecule – excluded volume between segments – repulsion between unlike species. How these properties are implemented in the computer model largely is a matter of numerical convenience and depends on which specific, non-universal properties (e.g., details of the local chain architecture) additionally shall be described.

A popular lattice model – the bond fluctuation model [3, 4] – is described in the left panel of Fig. 1. In this coarse-grained lattice model monomeric units are represented by unit cubes on a three-dimensional cubic lattice. Each monomer block the 8 sites of a cube from double occupancy. This mimics excluded volume interactions. Monomers along a polymer chain are connected via one of 108 bonding vectors that can adopt lengths, $l = 2, \sqrt{5}, \sqrt{6}, 3$, and $\sqrt{10}$ in units of the lattice spacing. This represents the connectivity along the polymer backbone. Monomers of the same type attract each other via a square well potential of depth $-\epsilon$ which is extended over the nearest 54 lattice sites. Unlike monomers repel each other via a potential of opposite sign. On the one hand, like other lattice representations the bond fluctuation models benefits from computational advantages (e.g., early rejection of forbidden moves) that allow for the simulation of rather large systems. On the other hand, the large number of bond vectors results in a rather good approximation of continuum properties.

However, if the density exhibits a sharp gradient – for instance, at a surface to vacuum or at a hard substrate – or liquid-crystalline order becomes important the structure of the underlying lattice might give rise to artefacts and off-lattice models are more adequate. A proto-typical off-lattice model is illustrated in the right panel of Fig. 1 [5, 6, 7]. Monomeric units along the

chain are bonded via a FENE-potential [5]:

$$V_{\text{FENE}}(r) = -kR_0^2 \ln(1 - \frac{r^2}{R_0^2}) \quad (3)$$

where $R_0 = 1.5\sigma$ and $k = 15\epsilon/\sigma^2$ are typical parameters. Monomeric units interact via a truncated and shifted Lennard-Jones potential of the form

$$V_{\text{LJ}}(r) = 4\epsilon \left\{ \left(\frac{\sigma}{r} \right)^{12} - \left(\frac{\sigma}{r} \right)^6 + \frac{127}{1024} \right\} \quad (4)$$

for $r < 2\sqrt[6]{2}$. The repulsive $1/r^{12}$ mimics the excluded volume of the monomeric units while the attractive $1/r^6$ -tail describes the attractive van-der-Waals interactions which make the polymers condense into a dense liquid. Thus, the interface between a dense polymer melt and its vapor (basically vacuum) can be investigated. σ and ϵ set the monomeric length and energy scale.

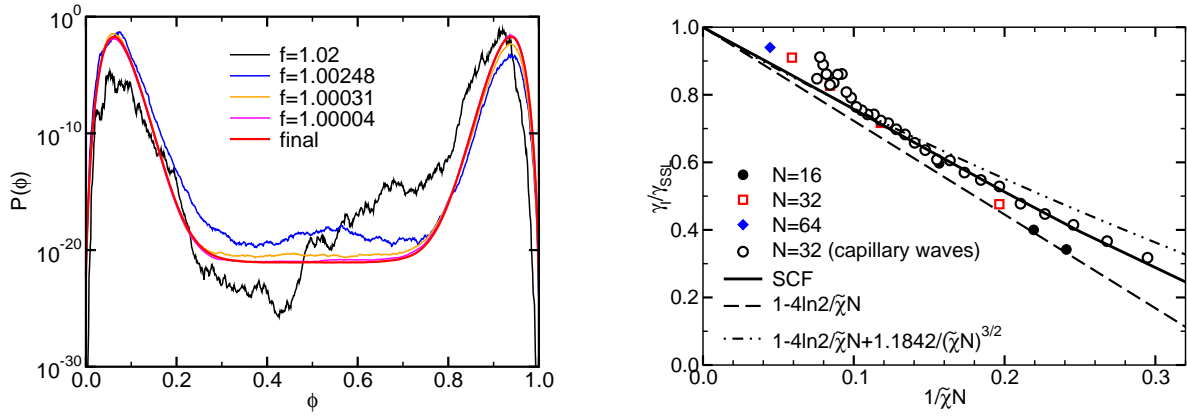


Fig. 2: (a) Probability distribution of the composition, φ_A , of a symmetric binary polymer blend within the framework of the bond fluctuation model [3]. The simulation data are obtained at the different stages of the Wang-Landau sampling [8] for chain length $N = 32$ and $\epsilon/k_B T = 0.02$ in a simulation cell of geometry $64 \times 64 \times 128$ in units of the lattice spacing ($R_e = 17$). The convergence factors, f , are indicated in the key. A flatness of 50% was required for the histogram of visited to particle numbers to reduce the convergence factor from $f \rightarrow f' = \sqrt{f}$. (b) Ratio between the interface tension γ_{AB} and the simple expression for the strong segregation limit γ_{SSL} in Eq. (31) as a function of inverse incompatibility. Symbols correspond to MC results for the bond fluctuation model, the solid line shows the result of the SCF theory, and the dashed line presents first corrections to the strong segregation limit. Adapted from [9].

Off-lattice models can be studied both by Monte Carlo simulations (see contribution by Vliegenthart) and Molecular dynamics (cf. article by Winkler). In this section I will focus on one particular technique to investigate phase and interfacial properties: multicanonical simulations [10]. To illustrate the method we consider a binary polymer blend that comprises two species A and B which are structurally symmetric (i.e., identical chain architecture) but repel each other with strength χN . At low temperatures, the two species will phase separate into domains that are rich in A -polymers and others where B -polymers are enriched. These domains are separated by interfaces. The two coexisting phases are distinguished by their composition, φ_A . To investigate the properties of the symmetric mixtures one utilizes the semi-grandcanonical ensemble [11] where the temperature, T , volume, \mathcal{V} , and total number of chains, $n_A + n_B$,

are fixed. The composition, $\varphi_A \equiv \frac{n_A}{n_A+n_B}$, however, fluctuates and one controls the thermodynamically conjugated exchange potential, $\Delta\mu$. A Monte Carlo simulation that realizes this ensemble comprises moves that update the polymer conformations and, additionally, moves that “mutate” an A -polymer into a B -polymer and vice versa. For a structurally symmetric blend this amounts merely to exchanging the label of the monomeric units at fixed conformation and the move is accepted with the Metropolis acceptance probability $\min[1, \exp(-\Delta E_{A \rightleftharpoons B}/k_B T)]$ where $\Delta E_{A \rightleftharpoons B}$ denotes the energy change associated with the exchange of labels. The key quantity to monitor is the probability distribution $P(\varphi_A)$ of the composition which is presented in Fig. 2(a). At coexistence, it exhibits two peaks at values that correspond to the compositions of the two coexisting phases. The two phases coexist at a chemical potential $\Delta\mu$ if they have equal (semi-grandcanonical) free energy (equivalent to pressure). Since the free energy of a phase is proportional to the logarithm of the weight of the corresponding peak of $P(\varphi_A)$ the phase coexistence can be accurately located by the equal weight criterion [12, 13]:

$$\int_0^{\varphi_A^*} d\varphi_A P_{T,\Delta\mu_{\text{coex}}}(\varphi_A) \stackrel{!}{=} \int_{\varphi_A^*}^1 d\varphi_A P_{T,\Delta\mu_{\text{coex}}}(\varphi_A) \quad (5)$$

Where one cuts the distribution, φ_A^* , to distinguish the two phases is not important because the probability between the two peaks exponentially decreases with system size. Configurations with $\varphi_A \approx \varphi_A^*$ consists of two slab-like domains that are separated by two AB interfaces from each other. Let L^2 denote the cross-sectional area of the simulation cell and γ_{AB} the interface tension then the probability of those slab-like configurations is suppressed by a factor $\exp(-2L^2\gamma_{AB}/k_B T)$ compared to homogenous bulk configurations. This can be exploited to calculate the interface tension via [14]:

$$\gamma_{AB} = \frac{k_B T}{2L^2} \ln \frac{P(\varphi_A^{\text{coex}})}{P(\varphi_A^*)} \quad (6)$$

The plateau in the distribution P around φ_A^* implies that one can change φ_A and thereby change the distance between the two interfaces at no free energy cost, i.e., the two interfaces do not interact [15] and the excess free energy can be described by two non-interacting interfaces of area L^2 .

If this excess free energy is large, the probability around φ_A^* is very small and the system will not make transitions from one phase to the other in the course of a simulation in the semi-grandcanonical ensemble. In order to sample states inside the miscibility gap one has to modify the statistical weights of these configurations in a multicanonical way. To this end one samples in the simulations not according to the Boltzmann weight but utilizes the partition function [10, 15]

$$\mathcal{Z}_{\text{muca}} = \frac{1}{n_A!n_B!} \sum_{n_A=n-n_B=0}^n \int \mathcal{D}_A[\mathbf{r}] \mathcal{D}_B[\mathbf{r}] e^{-w(n_A)} e^{-E/k_B T} \quad (7)$$

where the weights, $w(n_A)$, depend on the number of A -polymers but not on the polymer conformations. If one could choose $w(n_A) = \ln P(n_A)$ the simulation would uniformly sample the entire composition interval. Unfortunately, $\ln P(n_A)$ is unknown – it is the result of the simulation – and thus one needs a good estimate. There are several schemes which provide practical estimates: multicanonical recursion [10], successive umbrella sampling [16, 17] or the Wang-Landau algorithm [8]. The latter method is illustrated in Fig. 2(a).

The results of such a simulation is the accurate location of the phase coexistence (i.e., coexistence densities and chemical potentials or pressure), the fluctuations in the homogeneous phase

(i.e., compressibility) and the interface tension. The results for the latter quantity are shown in panel (b) of Fig. 2 and will be discussed in Sec. 2.5.

2.2 Self-consistent field (SCF) theory

In the self-consistent field theory [18, 19, 20, 21, 22, 23, 24] one replaces the problem of many mutually interacting chains by much simpler problem of a single chain in an external field. The external field mimics the interactions with the surrounding molecules. Since one molecule interacts with many neighbors ($\mathcal{O}(\bar{N})$) the fluctuations of the interactions that an entire molecule is exposed to are small and, thus, can be faithfully approximated by a mean field. It is thought that the SCF theory can quantitatively describe properties on the scale of the polymer coil in the limit $\bar{N} \rightarrow \infty$.

The starting point of the field-theoretic description of a binary polymer blend is the partition function:

$$\mathcal{Z} \sim \frac{1}{n_A!n_B!} \int \mathcal{D}_A[\mathbf{r}] \mathcal{P}_A[\mathbf{r}] \mathcal{D}_B[\mathbf{r}] \mathcal{P}_B[\mathbf{r}] \exp \left(-\frac{\mathcal{F}[\hat{\phi}_A, \hat{\phi}_B]}{k_B T} \right) \quad (8)$$

where $\mathcal{P}_A[\mathbf{r}]$ denotes the probability distribution of the non-interacting single chain conformations and the microscopic density of A -monomeric units is given by [18]

$$\hat{\phi}_A(\mathbf{r}) = \sum_{\alpha=1}^{n_A} \sum_{i=1}^N \delta(\mathbf{r} - \mathbf{r}_{\alpha,i}) \quad (9)$$

where $\mathbf{r}_{\alpha,i}$ denotes the position of the i th segment of A -molecules α . A similar definition holds for the microscopic density of B -segments.

A Hubbard-Stratonovich transformation allows to rewrite the partition function in terms of independent molecules in fluctuating, external fields, W_A and W_B :

$$\mathcal{Z} \sim \int \mathcal{D}W_A \mathcal{D}\Phi_A \mathcal{D}W_B \mathcal{D}\Phi_B e^{-\frac{\mathcal{G}[\Phi_A, \Phi_B, W_A, W_B]}{k_B T}} \frac{(\mathcal{Q}_A[W_A])^{n_A}}{n_A!} \frac{(\mathcal{Q}_B[W_B])^{n_B}}{n_B!} \quad (10)$$

$$\sim \int \mathcal{D}W_A \mathcal{D}\Phi_A \mathcal{D}W_B \mathcal{D}\Phi_B \exp \left(-\frac{F[\Phi_A, \Phi_B, W_A, W_B]}{k_B T} \right) \quad (11)$$

with

$$\frac{\mathcal{G}[\Phi_A, \Phi_B, W_A, W_B]}{k_B T} = \frac{\mathcal{F}[\Phi_A, \Phi_B]}{k_B T} - \int d\mathbf{r} [W_A \Phi_A + W_B \Phi_B] \quad (12)$$

$$\mathcal{Q}_A[W_A] = \frac{1}{\mathcal{V}} \int \mathcal{D}_{A,1} \mathcal{P}_{A,1} \exp \left[- \int d\mathbf{r} W_A(\mathbf{r}) \sum_{i=1}^N \delta(\mathbf{r} - \mathbf{r}_{1,i}) \right] \quad (13)$$

$$= \frac{1}{\mathcal{V}} \int \mathcal{D}_{A,1} \mathcal{P}_{A,1} \exp \left[- \sum_{i=1}^N W_A(\mathbf{r}_{1,i}) \right] \quad (14)$$

$$\frac{F[\Phi_A, \Phi_B, W_A, W_B]}{k_B T} = n_A \ln \frac{n_A/\mathcal{V}}{e \mathcal{Q}_A[W_A]} + n_B \ln \frac{n_B/\mathcal{V}}{e \mathcal{Q}_B[W_B]} + \frac{\mathcal{G}[\Phi_A, \Phi_B, W_A, W_B]}{k_B T}$$

$\mathcal{Q}_A[W_A]$ is the single molecule partition function in the external field, W_A , and the functional integral $\mathcal{D}_{A,1}$ only sums over the conformation of a single A -molecule. A similar expression

holds for the partition function of a single B -molecule, $\mathcal{Q}_B[W_B]$, in the external field, W_B . This reformulation of the partition function, Eq. (8), of the interacting multi-chain system in terms of independent molecules in external, but fluctuating fields, W_A and W_B , is formally exact but it merely shifts the problem to the evaluation the functional integral over the fluctuating fields. In the SCF theory one replaces those integrals by their saddle-point values which are denoted by lower-case letters:

$$\frac{1}{k_B T} \frac{\delta F[\phi_A, \phi_B, w_A, w_B]}{\delta w_A(\mathbf{r})} = -\frac{n_A}{\mathcal{Q}_A} \frac{\delta \mathcal{Q}_A}{\delta w_A(\mathbf{r})} - \phi_A \equiv \phi_A^*[W_A](\mathbf{r}) - \phi_A = 0 \quad (15)$$

The saddle point value of the collective density, ϕ_A , is given by the density, $\phi_A^*[w_A](\mathbf{r})$, a single A -molecule creates if all conformations are weighted by the Boltzmann factor that corresponds to its energy in the external field, w_A .

$$\begin{aligned} \phi_A^*[w_A](\mathbf{r}) &= -\frac{n_A/\mathcal{V}}{\mathcal{Q}_A} \frac{\delta}{\delta w_A(\mathbf{r})} \int \mathcal{D}_{A,1} \mathcal{P}_{A,1} \exp \left[- \int d\mathbf{r} w_A(\mathbf{r}) \sum_{i=1}^N \delta(\mathbf{r} - \mathbf{r}_{1,i}) \right] \\ &= \frac{n_A/\mathcal{V}}{\mathcal{Q}_A} \int \mathcal{D}_{A,1} \mathcal{P}_{A,1} \sum_{i=1}^N \delta(\mathbf{r} - \mathbf{r}_{1,i}) \exp \left[- \int d\mathbf{r} w_A(\mathbf{r}) \sum_{i=1}^N \delta(\mathbf{r} - \mathbf{r}_{1,i}) \right] \end{aligned} \quad (16)$$

$$= n_A \left\langle \sum_{i=1}^N \delta(\mathbf{r} - \mathbf{r}_{1,i}) \right\rangle_{\text{single } A\text{-molecule in external field, } w_A} \quad (17)$$

The saddle point condition for the collective density, Φ_A , reads:

$$-\frac{1}{k_B T} \frac{\delta F[\phi_A, \phi_B, w_A, w_B]}{\delta \phi_B(\mathbf{r})} = w_A - \frac{1}{k_B T} \frac{\delta \mathcal{F}[\phi_A, \phi_B]}{\delta \phi_A(\mathbf{r})} = 0 \quad (18)$$

This expression provides an explicit relation between the external field, w_A , which acts on an A -segment and which mimics the effect of all surrounding molecules of the corresponding interacting multi-chain system, and the local densities, ϕ_A and ϕ_B . The average density of B -molecules and the external field, which mimics the interactions of the other molecules on them, is given by expressions similar to Eqs. (17) and (18). Inserting the saddle point values, ϕ_A , ϕ_B , w_A and w_B into the free energy functional F one estimates the free energy.

To complete the description one has to specify the chain model which is encoded in the probability distributions, $\mathcal{P}_A[\mathbf{r}]$ and $\mathcal{P}_B[\mathbf{r}]$, of the non-interacting polymer species and the interaction free energy functional, $\mathcal{F}[\hat{\phi}_A, \hat{\phi}_B]$. The latter incorporates all the microscopic information and therefore one often utilizes a simple form that employs a zero-ranged repulsion of strength χ and replaces the excluded volume interaction via a compressibility constraint [18].

$$\frac{\mathcal{F}[\varphi_A, \varphi_B]}{k_B T} = -\frac{\chi \rho}{4} \int d\mathbf{r} [\varphi_A(\mathbf{r}) - \varphi_B(\mathbf{r})]^2 + \frac{\kappa \rho}{2} \int d\mathbf{r} [\varphi_A(\mathbf{r}) + \varphi_B(\mathbf{r}) - 1]^2 \quad (19)$$

where we have used the composition, $\varphi_A \equiv \phi_A/\rho$ instead of the density, ϕ_A . The parameter κN has to be chosen large enough to suppress fluctuations of the total density. By the same token, one utilizes a computationally convenient chain model – the Gaussian chain model – which suffices to capture the conformational statistics on the scale R_e .

$$\mathcal{P}_{A,1}[\mathbf{r}(\tau)] \sim \exp \left[-\frac{3}{2R_e^2} \int_0^1 d\tau \left(\frac{d\mathbf{r}}{d\tau} \right)^2 \right]. \quad (20)$$

The parameter $0 \leq \tau \leq 1$ parameterizes the continuous polymer conformations. This form emphasizes that the discretization, N , along the chain does not have a physical meaning and it allows to make analytical progress. To this end, one defines the probability $q(\mathbf{r}, s)$ that a chain fraction of length $0 \leq s \leq 1$ ends at position $\mathbf{r}(s) = \mathbf{r}$.

$$q_A(\mathbf{r}, t) = \int_0^t \mathcal{D}_{A,1}[\mathbf{r}] \mathcal{P}_{A,1}[\mathbf{r}] \delta(\mathbf{r}(t) - \mathbf{r}) e^{-\int_0^t d\tau N w_A(\mathbf{r}(\tau))} \quad (21)$$

This end segment distribution obeys the following diffusion equation [18]

$$\frac{\partial q_A(\mathbf{r}, t)}{\partial t} = \frac{R_e^2}{6} \nabla^2 q_A(\mathbf{r}, t) - N w_A(\mathbf{r}) q_A(\mathbf{r}, t) \quad (22)$$

with the boundary condition $q_A(\mathbf{r}, 0) = 1$, i.e., the beginning of the chain fragment is uniformly distributed. Once this partial differential equation is solved the composition can be obtained from

$$\varphi_A(\mathbf{r}) = \frac{n_A N}{\rho Q_A} \int_0^1 dt q_A(\mathbf{r}, t) q_A(\mathbf{r}, 1 - t) \quad (23)$$

and the single chain partition function takes the form

$$Q_A = \frac{1}{V} \int d\mathbf{r} q_A(\mathbf{r}, 1) = \frac{1}{V} \int d\mathbf{r} q_A(\mathbf{r}, t) q_A(\mathbf{r}, 1 - t) \quad \forall t. \quad (24)$$

In the limit that the incompatibility between the two species is very weak $\chi N \ll 2$ or very strong $\chi N \gg 10$ the SCF theory allows to derive simple analytical expressions for structural and thermodynamic properties.

2.2.1 “Single-chain-in-mean-field”-simulations

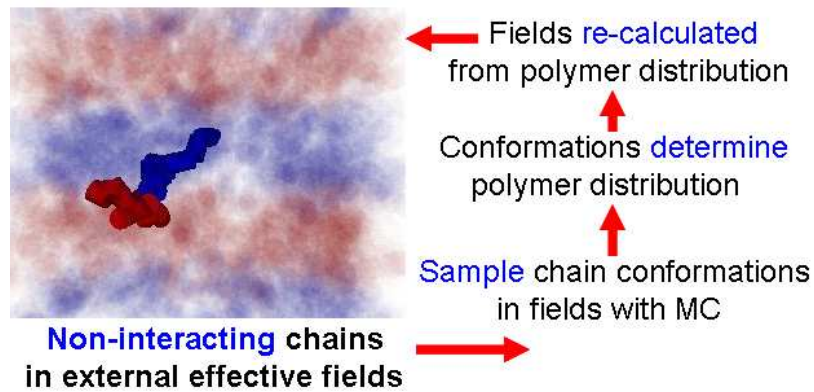


Fig. 3: Sketch of “Single-Chain-in-Mean-Field” (SCMF) simulations. See text for explanations.

The SCF theory in junction with the Gaussian chain model has found ample successful application to describe the structure and thermodynamics of polymer materials. However, it is rather difficult to incorporate additional details of the chain architecture, to describe fluctuations [25, 26, 24] or to investigate the collective dynamics of composition fluctuations in the

field-theoretical framework. For these issues particle-based SCF methods, like “single-chain-in-mean-field” simulations [27, 28], might offer advantages.

In this particle-based SCF method one considers an ensemble of independent chains in an external field. The explicit chain configurations are updated in the external fields via a standard Monte Carlo scheme utilizing local random displacements of the beads. After a small, predetermined number of Monte Carlo steps, the spatial density distribution created by the large ensemble of independent molecules is measured and the relation of the SCF theory between density and field (cf. Eq. (18)) is employed to calculate the new, external fields. Then, the process is iterated as illustrated in Fig. 3. In the limit of a very large ensemble of chains, fluctuations of the density and fields are vanishingly small and, in the stationary state, the chain configurations are in equilibrium with the external field. Thus both SCF equations, (17) and (18), are fulfilled and the stationary state of a large ensemble yields a solution of the SCF theory.

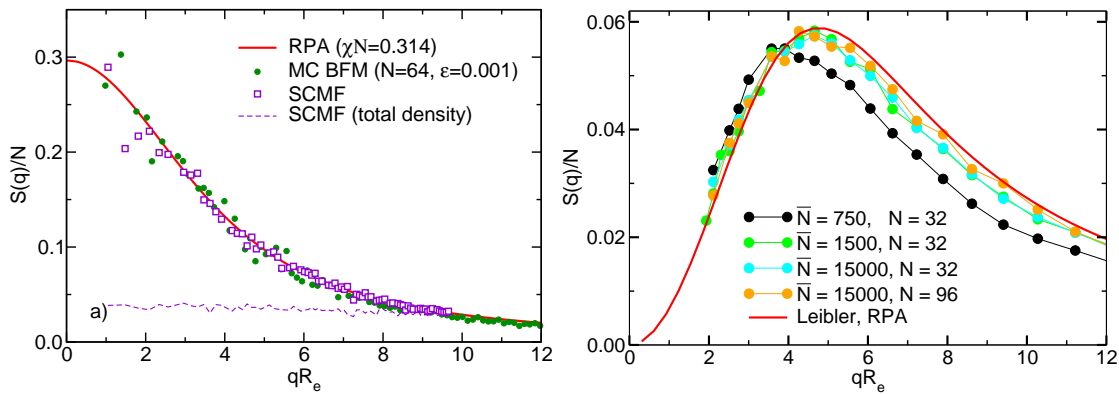


Fig. 4: (a) Equilibrium composition fluctuations of a symmetric binary polymer blend at $\chi N = 0.314$ as obtained from Random Phase Approximation, MC simulations of the bond fluctuation model, and SCMF simulations. The horizontal dashed lines also depicts the structure factor of the total density in the SCMF simulations which utilize a small but finite compressibility. From Ref. [27]. (b) Equilibrium composition fluctuations of a symmetric diblock copolymer at $\chi N = 2$ as obtained from SCMF simulations and Random Phase Approximation for a system of linear dimension, $L = 3R_e$. To achieve an invariant degree of polymerization of $\bar{N} = 15000$ (which corresponds to an intermediate molecular weight) in a typical bead spring model ($\rho = 0.83$) requires a large system of very long chains, i.e., 3400 chains each comprising $N = 3000$ beads. In the SCMF simulations we can reproduce these experimental values of \bar{N} simply by increasing the density rather than the chain discretization, N .

The particle-based method additionally offers advantages:

- The computational scheme utilizes coarse-grained polymer models (e.g., bead-spring model with bond angle potential [27]) and is not limited to the Gaussian chain model of the SCF theory. The use of explicit molecular conformations allows details of the chain architecture to be incorporated (e.g., stiffness along the backbone or branching).
- The density (and external fields) accurately mimic the instantaneous chain conformations. Numerical calculations for binary blends and diblock copolymers demonstrate that this simulation scheme can describe composition fluctuations (cf. Fig. 4) if the fields are updated frequently. This finding has been corroborated by approximate but analytical techniques [27].

- The explicit propagation of the chain conformations avoids the need of an Onsager coefficient [26] (cf. Fig. 6) and intramolecular correlations (that give rise to a non-local Onsager coefficient in field-theoretic schemes) are taken into due account.
- Propagating the explicit chain conformations in time we are able to investigate blends with strong dynamic asymmetries (e.g., where one component vitrifies during the phase separation process).
- Compared to computer models routinely utilized in Monte Carlo or Molecular Dynamics simulations (cf. Sec. 2) the methods allows to consider values of the invariant degree of polymerization, $\bar{N} \sim \mathcal{O}(10^5)$, that are typical for experimental systems.
- Furthermore, the scheme is computationally efficient, permits us to study large system sizes and it is suitable for parallel computers. To this end, we distribute the independent chain conformations evenly across the processors independent from their location in space. Each processor performs the Monte Carlo simulations for “its” molecules which are mutually independent but only interact with the external field. Each processor calculates the density of its molecules after the Monte Carlo simulation and the results are summed across the processors to construct the new external field for the next simulation.

In principle, one can use an arbitrary chain model in conjunction with the SCMF simulation. In the applications discussed in the next section we utilize the discretized Edwards model[29] which closely mimics the Gaussian chain model. The probability distribution of A -molecule α with segment positions, $\mathbf{r}_{\alpha,1}, \dots, \mathbf{r}_{\alpha,N}$ are described by:

$$\mathcal{P}_{A,\alpha}[\mathbf{r}_\alpha] \sim \prod_{i=1}^{N-1} \exp \left[-\frac{3(\mathbf{r}_{\alpha,i} - \mathbf{r}_{\alpha,i+1})^2}{2b^2} \right] \quad (25)$$

with $b^2 = R_e^2/(N-1)$ being the statistical segment length. B -molecules obeyed the same segment distribution. The segment interaction in a binary blend is given by Eq. (19) and the explicit form of the effective field, w_A , acting on an A -segment at position \mathbf{r} simply is

$$w_A(\mathbf{r}) = -\frac{\chi}{2} [\varphi_A(\mathbf{r}) - \varphi_B(\mathbf{r})] + \kappa [\varphi_A(\mathbf{r}) + \varphi_B(\mathbf{r}) - 1]. \quad (26)$$

2.3 Applications

We can address two types of questions by quantitatively comparing computer simulations of coarse-grained, particle-based polymer models with SCF theory: (i) How to identify the coarse-grained parameter, χN , for a specific, particle-based model? For which properties and parameters is the coarse-grained description of the polymer conformations by the Gaussian chain model valid? For which aspects are microscopic properties of the underlying model important? (ii) What is the validity of the mean field approximation (or additional approximations invoked in less accurate analytical treatments of the field theoretical model)? Once the validity of the SCF approach is established it can be utilized to explore the behavior of larger or more complex systems.

2.4 Phase behavior of homopolymer blends

In simulations as well as in experiments it is common practice to measure the Flory-Huggins parameter by comparing the results of the simulations to the predictions of the mean field theory.

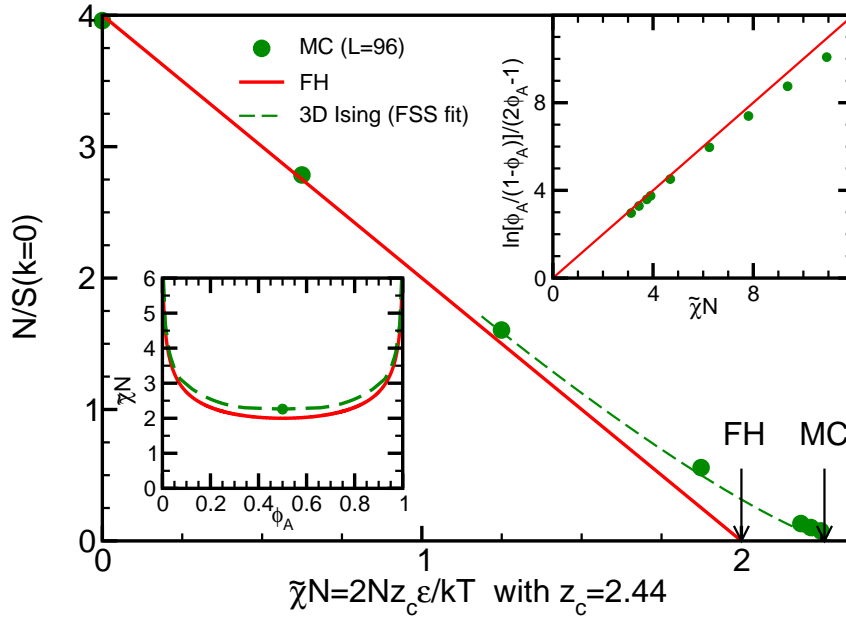


Fig. 5: Inverse maximum of the collective structure factor of composition fluctuations, $N/S(k \rightarrow 0)$, as a function of the incompatibility, χN . Symbols correspond to MC simulations of the bond fluctuation model, the dashed curve presents the results of a finite size scaling analysis of the simulation data in the vicinity of the critical point, and the straight, solid line indicates the prediction of the Flory-Huggins theory. The critical incompatibility, $\chi_c N = 2$ predicted by the Flory-Huggins theory and obtained from Monte Carlo simulations of the bond fluctuation model ($\bar{N} \approx 240$, $N = 64$, $\rho = 1/16$ and $R_e = 25.12$) are indicated by arrows. The left inset compares the phase diagram obtained from simulations with the prediction of the Flory-Huggins theory (cf. Eq. (2)). The right inset replots the compositions at coexistence such that the mean field theory predicts them to fall onto a straight line. From Müller [30].

Since the predictions are affected by fluctuation effects to different extents, not all quantities yield mutually compatible estimates of the Flory-Huggins parameter, χ .

From the Flory-Huggins free energy of mixing (cf. Eq. (2)) one readily calculate the binodals (composition of the two coexisting phases)

$$\ln \frac{\phi}{1-\phi} + \chi N(1-2\phi) = \frac{\Delta\mu_{\text{coex}}}{k_B T} = 0, \quad (27)$$

the location of the critical point, $\chi_c N = 2$ and $\phi_c = 1/2$, which marks the onset of phase separation, and the strength of composition fluctuations in the one phase region

$$\frac{N}{S(k \rightarrow 0)} = \frac{1}{\phi} + \frac{1}{1-\phi} - 2\chi N \quad \text{for} \quad \chi N < 2 \quad (28)$$

as measured by the structure factor $S(k)$ of composition fluctuations in the limit that the wavevector k vanishes. The last quantity is very popular to determine the Flory-Huggins parameter for miscible blends.

A comparison between the mean field prediction and the Monte Carlo results is presented in Fig. 5. The main panel plots the inverse scattering intensity vs. χN . At small incompatibility the simulation data are compatible with a linear prediction (cf. Eq. (28)) and from the slope one can estimate the relation between the Flory-Huggins parameter χ and the depth of the square well potential, ϵ in the simulations of the bond fluctuation model [13, 4]. As one approaches the critical point of the mixture deviations between the predictions of the mean field theory and the simulations become apparent because the theory cannot capture the strong universal (3D Ising-like) composition fluctuations at the critical point [11, 31, 32] and it underestimates the incompatibility necessary to bring about phase separation. If we fitted the behavior of composition fluctuations at criticality to the mean field prediction we would obtain a quite different estimate for the Flory-Huggins parameter. This estimate, however, would not well characterize the incompatibility between the polymer species but rather quantify the inability of the mean field theory to cope with Ising-like order parameter fluctuations.

The insets of Fig. 5 show the binodals of the symmetric blend. Again we find deviations in the ultimate vicinity of the critical point but for larger incompatibilities $\chi N \gg 2$ the mean field predictions provides an adequate description of the phase boundary utilizing the Flory-Huggins parameter extracted from the composition fluctuations in the one phase region, $\chi N < 2$.

If we quench the system from the one-phase region deep into the miscibility, composition fluctuations spontaneously grow (early stages of spinodal decomposition) according to

$$S(\mathbf{k}, t) = S_{\chi_0 N}(\mathbf{k}) \exp(R(\mathbf{k})t) \quad (29)$$

where S denotes the collective structure factor of composition fluctuations

$$\frac{S(\mathbf{k}, t)}{N} = \frac{1}{\sqrt{\mathcal{N}}(\mathcal{V}/R_e^3)} \left\langle \left| \int d\mathbf{r} \hat{\varphi}_A(\mathbf{r}) \exp(i\mathbf{r}\mathbf{k}) \right|^2 \right\rangle \quad (30)$$

In Fig. 6 the growth rate, $R(k)$, in response to a temperature quench from the one-phase region, $\chi N = 0.314$ into the miscibility gap, $\chi N = 5$ is presented as observed in Monte Carlo simulations of the bond fluctuation model, dynamic SCF calculations [26] and SCMF simulations [27]. The growth rate, $R(k)$, comprises a thermodynamic factor that is determined by the equilibrium

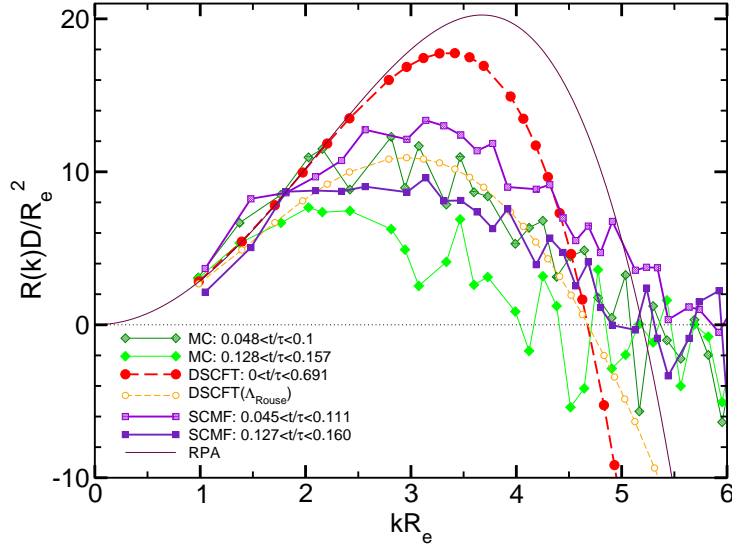


Fig. 6: Growth rate, $R(k)\tau$, of the collective structure factor, $S(k) \sim \exp[R(k)t]$, as a function of the wavevector, k . Data from MC simulations of the bond fluctuation model at an early and intermediate time regime and the results from the dynamic SCF theory using a local and a Rouse-like Onsager coefficient are adapted from Ref. [26]. The results of the SCMF simulations slightly overestimate the initial growth rate at large wavevectors, but capture the fastest growing mode, the decrease of the rate with time and do not predict negative rates (damping) at high wavevectors in agreement with the MC simulations. The prediction of the Random Phase Approximations is also included as thin solid line. Adapted from Müller and Smith [27]

thermodynamics of the mixture and an Onsager coefficient that relates the kinetics of collective concentration fluctuations to the dynamics of the polymers. Due to the extended shape of the macromolecules the Onsager coefficient is non-local and explicit expressions exist for the homogeneous system [33]. Fig. 6 clearly demonstrates that a local Onsager coefficient fails to describe the simulation results, but dynamic SCF calculations using a non-local Onsager coefficient [26] and SCMF simulations that do not utilize an Onsager coefficient but rather propagate the explicit chain conformations in time yield an improved description.

It is also instructive to compare the computational effort between the different schemes: For the MC simulations of 64 independent systems over the time interval 0.33τ a computational effort of 40 days on 64 processors of a CRAY T3E was needed. Using $7 \times 7 \times 7 = 343$ grid points in Fourier space the corresponding dynamic SCF calculations required about 25 days on a CRAY J90. The single chain mean field calculations of 64 independent systems, each with twice as many polymers than in the MC simulations and a spatial resolution of 4096 grid points, took 19 hours on a 32×2 node Beowulf cluster of Opteron (1.8GHz) processors.

While explicit analytical expression for the non-local Onsager coefficient exist for spatially homogeneous systems (appropriate, e.g., for the early stages of spinodal decomposition), no such expression exist at spatial inhomogeneities (e.g., interfaces or surfaces). Under those circumstances the chain conformations are distorted and the calculation of the Onsager coefficient amounts to calculate intramolecular correlations which is computationally infeasible.

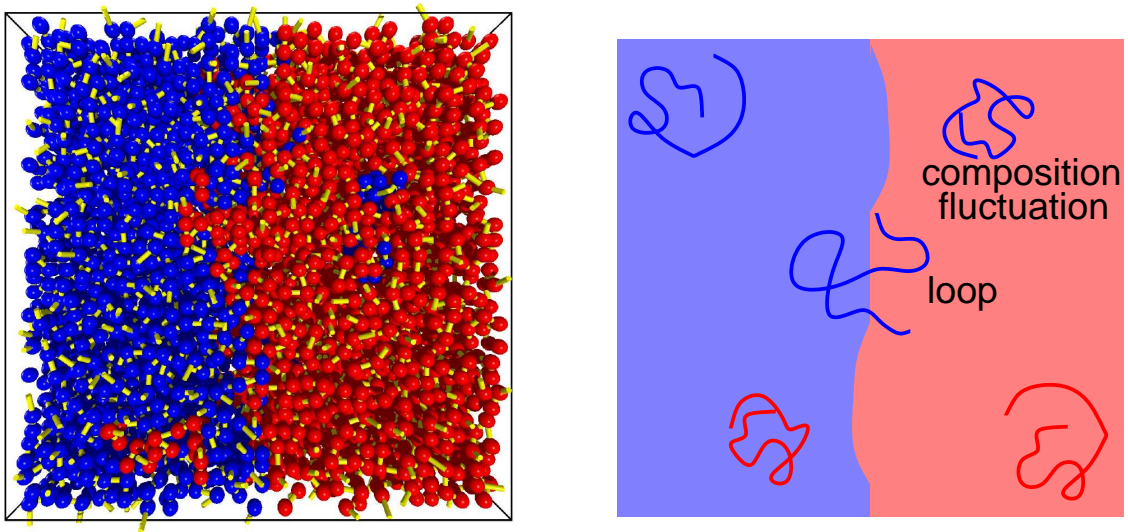


Fig. 7: (a) Snapshot of an interface between two coexisting phases in a binary polymer blend in the bond fluctuation model (invariant polymerization index $\bar{N} = 91$, incompatibility $\chi N \approx 17$, linear box dimension $L \approx 7.5R_e$, or number of effective segments $N = 32$, interaction $\epsilon/k_B T = 0.1$, monomer number density $\rho = 1/16.0$). (b) Cartoon of the configuration illustrating loops of a chain into the domain of opposite type, fluctuations of the local interface position (capillary waves) and composition fluctuations in the bulk and the shrinking of the chains in the minority phase.

2.5 Interfacial properties

Properties of interfaces can broadly be divided into (i) excess properties (e.g., interface tension) and (ii) profiles of quantities across the interface. The former can straightforwardly be predicted by the SCF theory, the latter quantities are strongly affected by long-range fluctuations of the local interface position, i.e., capillary waves [34, 35, 36, 37].

The mean field theory suggests a simple picture of the structure of the interface between two immiscible polymers which is illustrated in Fig. 7. At the interface the long molecules loop into the opposite phase. The cost of each loop into the “hostile” phase is comparable to the thermal energy scale, $k_B T$. Each monomer along the loop contributes to this cost an amount $\chi k_B T$. Thus the typical number of monomers of a loop is $1/\chi$. If one assumes that loops contain many monomers and that the spatial statistics of loops corresponds to the Gaussian behavior of the entire coil the spatial extent of a loop is given by $w/R_e \sim (1/\chi)/N$. This characterizes the (intrinsic) width of the interface. This reasoning also explains why sharp interfaces between a polymer melt and its vapor or between very incompatible polymer species (i.e., $\chi \sim \mathcal{O}(1)$) cannot be described by the Gaussian chain model. In this case the width of the interface is comparable to the statistical segment length and one has to account for non-universal, specific molecular architecture.

Each monomer within this interfacial zone contributes to the free energy cost of the interface an amount χ . The free energy per unit area can be calculated to $\gamma \sim \rho w \chi$. The mean field theory corroborates this simple picture of the interface at strong segregation ($1 \ll \chi N \ll N$) and yields [18]

$$\gamma_{\text{SSL}} = \rho R_e \sqrt{\chi/6N} = \frac{\sqrt{N}}{R_e^2} \sqrt{\chi N/6} \quad (31)$$

This estimate has been used to normalize the interface tension in Fig. 2. The collapse of the data for different chain lengths onto a common curve shows that the interface tension indeed only depends on the combination χN and the data are well described by numerical self-consistent field calculations [9] and analytic prediction by Semenov [38] using the identification of the Flory-Huggins parameter from the bulk properties.

If we wish to compare profiles across the AB interface, we encounter a fundamental difficulty. In the SCF theory the interface is perfectly flat; this is, indeed, the most probable configuration. In simulations (cf. Fig. 7(a)) or experiments, however, the local interface position fluctuates. Those thermal fluctuations cost vanishingly little energy in the long-wavelength limit. A snapshot of a coarse-grained local interface position $u(x, y)$ (where x and y denote the two coordinate parallel to the interface) is presented in Fig. 8(a) for a symmetric blend with chain length $N = 32$ in the bond fluctuation model [39]. Such fluctuations of the local interface position will broaden the profiles measured in experiments or simulations.

In the simulations [42, 41, 39] one can measure the local interface position $z = u(\mathbf{x})$ as a function of the two coordinates, $\mathbf{x} = (x, y)$, parallel to the (average) interface plane (Monge representation). At this stage, we assume that the configuration does not contain bubbles or overhangs. This can be achieved by smoothing the composition profile over a microscopic length scale. Rather than describing the configuration by a detailed, particle-based model which describes the location and conformations of the molecules in space, we just characterize the configuration by the location, $u(\mathbf{x})$, of the interface.

On large lateral length scales, the effect of the fluctuations of the local interface position is to increase the area of the interface, and the free energy cost can be described by the capillary

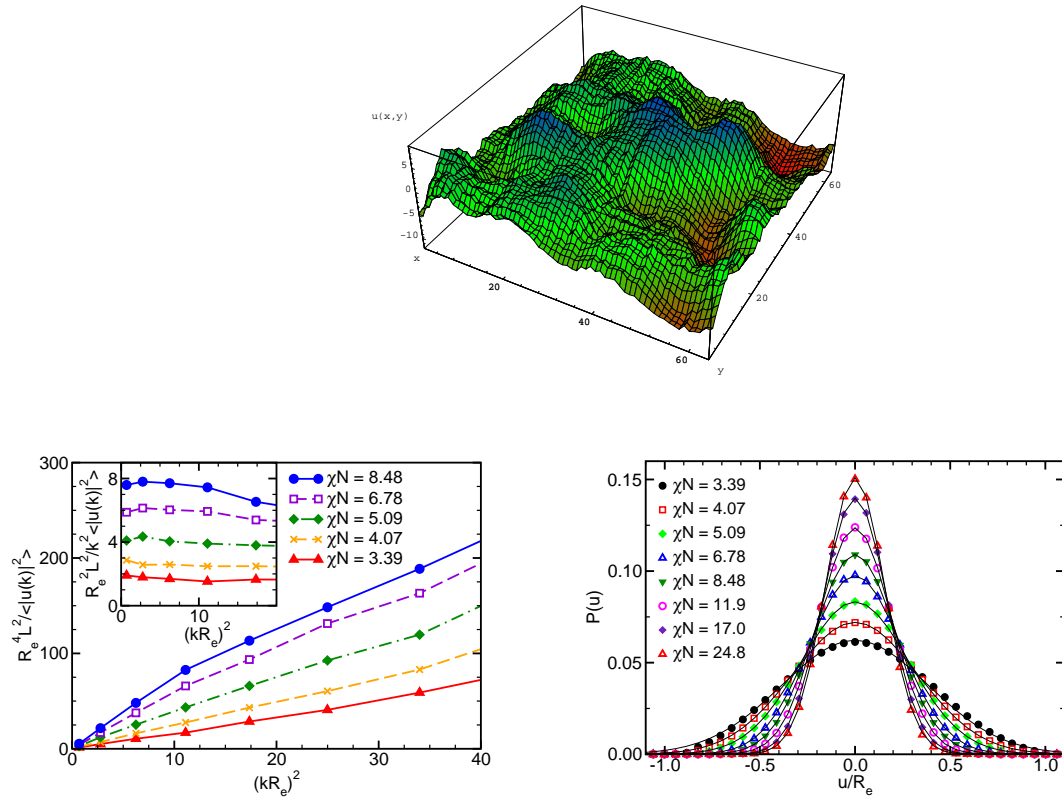


Fig. 8: (a) Snapshot of the local interface position obtained from MC simulations in the framework of the bond fluctuation model ($\bar{N} = 91$, $\chi N = 5.09$, $L = 3.77R_e$). The local interface position is determined by analyzing the profiles on a lateral length scale $B = 0.47R_e$. Adapted from [39]. (b) Spectrum of interface fluctuations for different incompatibilities as indicated in the key. The inset shows the wavevector dependence of the interface tension. (c) Probability distribution of the local interface position for different incompatibilities. Adapted from [40].

wave Hamiltonian $\mathcal{H}[u(\mathbf{x})]$ [34, 35, 36, 37]:

$$\mathcal{H}[u(\mathbf{x})] = \gamma_{AB} \int d^2\mathbf{x} \left(\sqrt{1 + (\nabla u)^2} - 1 \right) \approx \frac{\gamma_{AB}}{2} \int d^2\mathbf{x} (\nabla u)^2 \quad (32)$$

where γ_{AB} denotes the interface tension, and the integration is extended over the projected area, $L \times L$. From this capillary wave Hamiltonian, we can estimate the fluctuations of the local interface position. Utilizing the Fourier spectrum of interface fluctuations, $u(\mathbf{k})$,

$$u(\mathbf{x}) = \frac{1}{L^2} \sum_{\mathbf{k}} u(\mathbf{k}) \exp(i\mathbf{k} \cdot \mathbf{x}) = \frac{1}{(2\pi)^2} \int d^2\mathbf{k} u(\mathbf{k}) \exp(i\mathbf{k} \cdot \mathbf{x}) \quad (33)$$

$$u(\mathbf{k}) = \int d^2\mathbf{x} u(\mathbf{x}) \exp(-i\mathbf{k} \cdot \mathbf{x}) \quad (34)$$

one diagonalizes the capillary wave Hamiltonian.

$$\mathcal{H}[u(\mathbf{k})] = \frac{\gamma_{AB}}{2} \frac{1}{(2\pi)^2} \int d^2\mathbf{k} k^2 |u(\mathbf{k})|^2 \quad (35)$$

The statistical mechanics of the interface position can be described by the partition function

$$\mathcal{Z}_{\text{int}} = \int \mathcal{D}[u] \exp \left(-\frac{\mathcal{H}[u]}{k_B T} \right) \quad (36)$$

where the functional integral $\int \mathcal{D}[u]$ sums over all local positions of the interface. Since the Hamiltonian is the sum of independent, quadratic degrees of freedom, $u(\mathbf{k})$, the Fourier modes are uncorrelated and Gaussian distributed around zero and their variance is given by the equipartition theorem:

$$\frac{\gamma_{AB}}{L^2} k^2 \langle |u(\mathbf{k})|^2 \rangle = k_B T \quad (37)$$

The spectrum of interface fluctuations is shown in Fig. 8(b) as a function of the wavevector, k . When plotted as $R_e^4 L^2 / \langle |u(\mathbf{k})|^2 \rangle$ vs $(k R_e)^2$ the data for small wavevectors form a straight line, and one can extract the interface tension from the slope, $\gamma_{AB} R_e^2 / k_B T$. Indeed, this yields reliable results [42] that agree well with values determined independently from grandcanonical MC simulations and the predictions of the SCF theory (cf. Fig. 2).

Utilizing this result we obtain for the fluctuations of the local interface position in a lateral patch of size $L \times L$:

$$\begin{aligned} \langle u^2(\mathbf{x}) \rangle_L &= \frac{1}{(2\pi)^4} \int d^2\mathbf{k} d^2\mathbf{k}' \langle u(\mathbf{k}) u(\mathbf{k}') \rangle \exp(i\mathbf{k}\mathbf{x} + i\mathbf{k}'\mathbf{x}) \\ &= \frac{1}{(2\pi)^2} \int d^2\mathbf{k} \frac{k_B T}{\gamma_{AB} k^2} = \frac{k_B T}{2\pi \gamma_{AB}} \int_{k_{\min}}^{k_{\max}} dk \frac{1}{k} \\ &= \frac{k_B T}{2\pi \gamma_{AB}} \ln \frac{k_{\max}}{k_{\min}} \end{aligned} \quad (38)$$

Since the integral over the magnitude of the wavevector diverges logarithmically, we have introduced an upper and a lower cut-off, k_{\min} and k_{\max} . The lower cut-off is set by the lateral system size, $k_{\min} = 2\pi/L$ or the lateral coherence length in a scattering experiment. The upper cut-off is more subtle, it marks the lateral length scale, where the description of fluctuations via

the capillary Hamiltonian (32) breaks down and the intrinsic structure of the interface becomes important [43], and we shall investigate this issue further below.

The distribution of the local interface position is presented in Fig. 8(c). Indeed, the fluctuations are Gaussian distributed and the variance increases as we decrease the incompatibility,

$$P_L(u) = \frac{1}{2\pi\langle u^2 \rangle_L} \exp\left(-\frac{u^2}{2\langle u^2 \rangle_L}\right) \quad (39)$$

To describe the profile, $p_{Q,L}(z)$, of a quantity, Q , measured in simulations and experiments on a lateral length scale L and to compare it with the prediction of the SCF theory, one has to account for the fluctuation of the interface position. If the interface position, $u(x, y)$, were fixed, the quantity Q would approximately be describable by

$$p_Q(x, y, z) = p_{Q,\text{intr}}(z - u(x, y)) \quad (40)$$

where $p_{Q,\text{intr}}(z)$ is the profile of quantity Q across a hypothetically flat interface and z denotes the coordinate normal to that interface. It is this quantity that can be calculated by the SCF theory and we refer to it as the “intrinsic” profile. Averaging this expression over the distribution of the local interface positions, $P_L(u)$, we arrive at the convolution approximation for the apparent profile [43]:

$$p_{Q,L}(z) = \int du P_L(u) p_{Q,\text{intr}}(z - u) \quad (41)$$

To estimate the qualitative effect, we assume that the “intrinsic” profile, $p_{Q,\text{intr}}$ varies smoothly on the scale $\langle u^2 \rangle_L$. Then, one can expand $p_{Q,\text{intr}}(z - u)$ around $u = 0$, and obtains to lowest order [44]:

$$p_{Q,L}(z) = p_{Q,\text{intr}}(z) + \frac{1}{2}\langle u^2 \rangle_L \frac{d^2 p_{Q,\text{intr}}(z)}{dz^2} + \mathcal{O}(\langle u^4 \rangle_L) \quad (42)$$

The intrinsic composition profile across the interface is describable by a tanh-form or an error function:

$$p_{\varphi,\text{intr}}(z) \approx \frac{1}{2} + \frac{2\bar{\varphi}_{\text{Acoex}} - 1}{2} \tanh\left(\frac{z}{w_{\text{intr}}}\right) \quad (43)$$

$$\approx \frac{1}{2} + \frac{2\bar{\varphi}_{\text{Acoex}} - 1}{2} \text{erf}\left(\frac{\sqrt{\pi}z}{2w_{\text{intr}}}\right) \quad (44)$$

Both profiles provide a good description of the interface profile, and we have chosen the numerical coefficients such that the slope of both profiles at the center of the interface (i.e., at $z = 0$) coincide. The inverse of this slope at the center of the interface defines the width:

$$w \equiv \frac{2\bar{\varphi}_{\text{Acoex}} - 1}{2dp_{\varphi}(z=0)/dz} \quad (45)$$

The SCF theory predicts a tanh-profile for the “intrinsic” profile in the weak and the strong segregation limit.¹ The erf-profile will provide a good description of the apparent profile, if the “intrinsic” width is smaller than $\langle u^2 \rangle_L$.

¹At intermediate segregation, however, the interface profile is characterized by two length scales [45]. The intrinsic width, w_{intr} , which depends on χN and determines the slope of the profile at the center of the interface, and the bulk correlation length, $\xi \sim R_e$, which controls the approach of the profile to the composition of the coexisting phases in the wings of the profile.

Using the erf-profile we obtain for the broadening of the interface width [39]

$$w_L^2 = w_{\text{intr}}^2 + \frac{\pi}{2} \langle u^2 \rangle_L = w_{\text{intr}}^2 + \frac{k_B T}{4\gamma_{AB}} \ln \frac{L}{B_0} \quad (46)$$

where $B_0 = 2\pi/k_{\text{max}}$ defines the shortest length scale on which the description via the capillary wave Hamiltonian still holds. Note that the prefactor in front of the logarithmic term depends on the details of the interface profile (namely the third derivative at the center of the interface). Thus, the dependence of the apparent width of the interface is less accurate than the spectrum of interface fluctuations (cf. Fig. 8) for extracting the interface tension, γ_{AB} , from simulations or experiments.

Two remarks are in order: (i) If we measured the interface width in the natural length scale, R_e , we could rewrite Eq. (46) in the form:

$$\frac{w_L^2}{R_e^2} = f_w^2(\chi N) + \frac{1}{4\sqrt{N}f_\gamma(\chi N)} \ln \frac{k_{\text{max}}}{k_{\text{min}}} \quad (47)$$

where f_w and f_γ are functions of the incompatibility, χN , that approach for large χN the limits, $1/\sqrt{6\chi N}$ and $\sqrt{\chi N}/6$, respectively. In this formal sense, the broadening by capillary waves is a long-wavelength fluctuation: The saddle-point approximation invoked in the SCF theory neglects this fluctuation but, like other long-wavelength fluctuations (i.e., composition fluctuations in the vicinity of the critical point), the contribution of capillary waves to the width of the interface is only of the order $1/\sqrt{N}$. Nevertheless, in simulations [15, 39, 40] as well as in experiments [46, 47, 48], the broadening due to interface fluctuations often constitutes a significant fraction of the apparent width.

(ii) The equation (46) also points to a rather fundamental problem [40]: What is the significance of the “intrinsic” width that characterizes a hypothetical, perfectly flat interface? In simulations or experiments one can only measure the apparent width, w_L , of the interface as a function of the lateral length scale, L . Thus, in principle, it is impossible to disentangle the intrinsic width from the short length scale cut-off k_{max} . The binary polymer blend, however, offers an opportunity to go one step further: Assuming that the SCF theory quantitatively describes the intrinsic width and that we have accurately identified the Flory-Huggins parameter we can measure on which length scale, $1/k_{\text{max}}$, the simulation results coincide with the predictions of the SCF theory. This strategy yields a length scale, $1/k_{\text{max}} \approx w_{\text{SCF}}/2$, that is proportional to the intrinsic width of the interface [43, 40].

2.6 Self-assembly of diblock copolymers

Joining chemically distinct polymers – A and B – at their ends to form an AB diblock copolymer prevents macrophase separation of the two species. In order to reduce the number of energetically unfavorable interactions between distinct blocks in a melt, the molecules self-assemble into complex morphologies. The morphology is selected via a delicate balance between the free energy cost of the internal interfaces and the conformational entropy loss as the molecules stretch to fill space at constant density. The phase diagram in the bulk has been investigated in much detail as a function of the relative length of the blocks f and the incompatibility χN [49, 50, 22]. The morphologies found in copolymer melts and copolymer/homopolymer mixtures resemble the spatially structured phases of other amphiphilic systems (e.g., lipid/water mixtures).

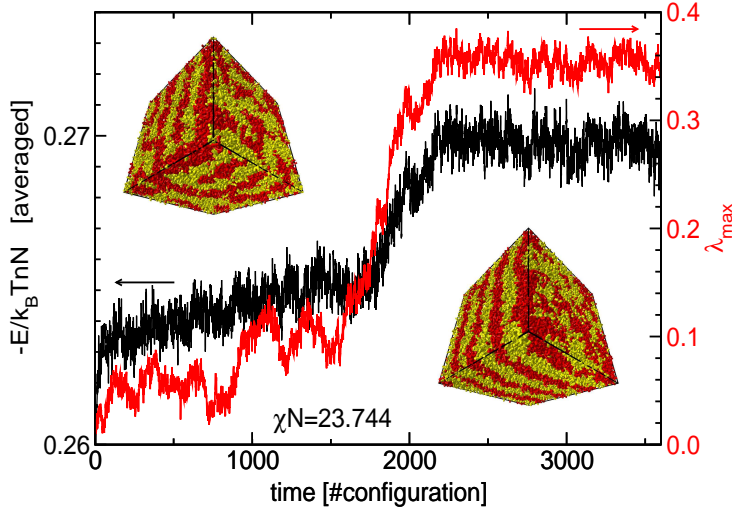


Fig. 9: Interaction energy (dark curve, left scale) and largest eigenvalue, λ_{\max} of the gyration tensor of the diblock copolymer as a function of time (in arbitrary units) for a quench from the disordered phase slightly below the ordering temperature obtained from simulations of the bond fluctuation model with $N = 32$, $\epsilon = 0.14$, and $L = 128$. The left snapshot presents the spatially structured but disordered morphology before the “jump” into the ordered phase which is depicted on the right hand side.

In this section we consider the structure and phase behavior of (nearly) symmetric diblock copolymers that form a lamellar phase in the bulk upon cooling. Within the SCF theory the transition for the disordered to the lamellar phase of a symmetric diblock copolymer is a second order phase transition [49] but fluctuations render it a first order transition [51]. This is illustrated in Fig. 9 which presents the energy and the largest eigenvalue of the molecules’ gyration tensor as the system is quenched from the disordered phase slightly below the order-disorder transition. The sudden change in the energy and elongation indicates the ordering. This is confirmed by the snapshots - on the left the system is spatially structured but disordered and on the right the system exhibits lamellar order spanning the entire simulation cell. The simulations of the bond fluctuation model correspond to an invariant degree of polymerization of $\bar{N} \approx 91$ and the first order transition occurs around $\chi_{\text{ODT}}N \approx 22$ which is larger than the prediction of the SCF theory $\chi_{\text{ODT}}N \approx 10.5$.

If one confines a lamellar forming diblock into a thin film the interplay between the natural periodicity of the lamellar bulk morphology and the finite film thickness, Δ , give rise to phase transition between different orientations of the lamellar morphology [52, 53, 54, 55, 56, 57]. The SCF prediction for the phase diagram as a function of the incompatibility, χN , and the film thickness Δ measured in units of the end-to-end distance is shown in Fig. 10. Away from the order-disorder transition (at $\chi N = 30$) the predicted morphologies agree with the simulation results (cf. snapshots on the left hand side of Fig. 10) and, taking due account of capillary waves, the SCF theory is able to additionally predict many features of the molecular arrangements (e.g., chain end distributions, orientations, etc) [56, 57].

We have used SCMF simulations to explore the self-assembly of copolymers and their mixtures with the corresponding homopolymers in nanopatterned substrates [58, 59, 28]. On patterned substrates the self-assembly is dictated by an intricate interplay between interfacial interactions, breaking of translational symmetry, and structural frustration due to the incompatibility between

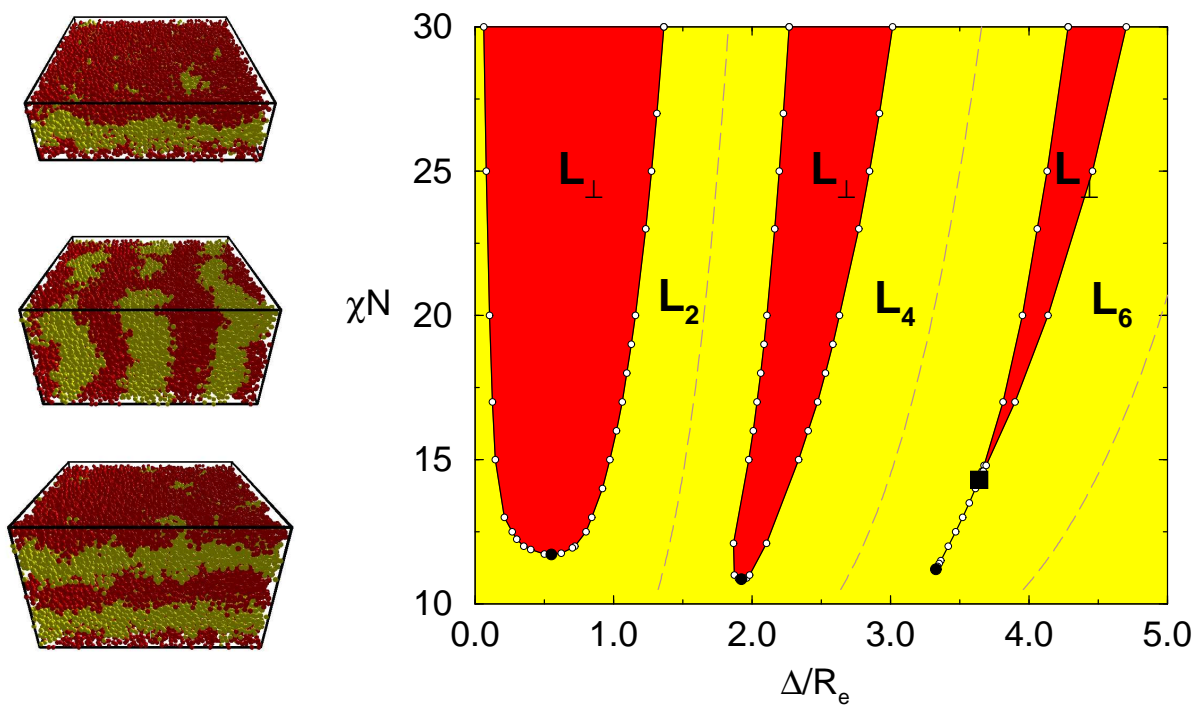


Fig. 10: Phase diagram of a thin film as a function of the incompatibility χN and the film thickness Δ/R_e . L_2 (upper left snapshot), L_{4i} (lower left snapshot), and L_6 denote parallel lamellar phases with 2, 4, and 6 AB interfaces, whereas L_\perp (middle snapshot) denotes the perpendicular lamellar phase. The dashed lines mark multiples of the bulk lamellar period. The square denotes the approximate location of the triple point where the L_4 , L_6 and L_\perp morphologies coexist. The circles mark the location of the (mean field) critical point from the disordered phase to the L_\perp phase. The snapshots on the right are obtained from MC simulations of the bond fluctuation model at $\chi N = 32$ and $\bar{N} \approx 91$. From Geisinger, Müller and Binder [56, 57].

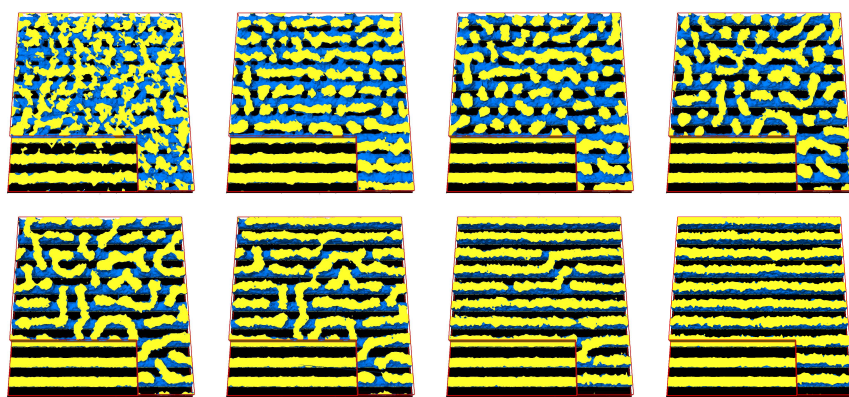


Fig. 11: Snapshot images of the three dimensional behavior of diblock copolymers on chemically nanopatterned substrates. The lateral system size is $17R_e \approx 0.5\mu\text{m}$. The time increases from left to right and from top to bottom. One component has been removed from the image and blue surfaces represent the interface between the different components. In the lower left corner 75% of the film has been removed to reveal the near-substrate morphology. From Ref. [58].

the natural periodicity of the bulk structure and film thickness and the substrate pattern. Confinement and surface effects can result in morphologies that are absent in the bulk, e.g., surface reconstructions [60].

Fig. 11 shows the ordering of a lamellar-forming diblock on top of a stripe pattern. There is a slight mismatch between the bulk lamellar period, $L_0 = 1.786R_e$ at $\chi N = 36.7$ and the pattern period, $L_S = 1.7R_e$. In the initial stage perfectly registered lamellae are formed at the substrate (substrate-directed ordering). The top (bulk) of the film, however, orders into microdomains later and those microdomains are not registered with the substrate pattern. Defects in the structure anneal not by lateral diffusion but the order of the registered lamellae propagates from the substrate to the top surface [58].

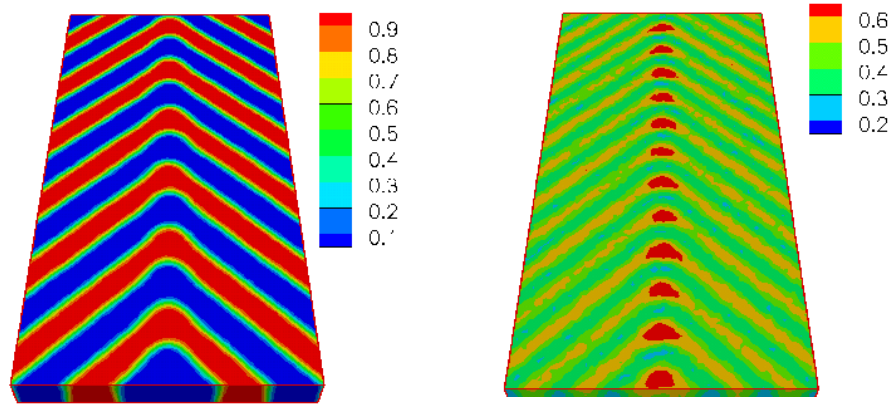


Fig. 12: *Three-dimensional contour plots of the composition (left) and the total homopolymer concentration (right) obtained from SCMF simulations. In the left panel the red and blue areas represent A- and B-rich domains, respectively. In the right panel, the periodic red areas are enriched alternatively in A and B homopolymers, whereas the blue stripes represent the domain interfaces that are depleted of homopolymers. From Ref. [59].*

It is of interest to explore what geometrical patterns can be reproduced by diblock copolymer materials. Generally, only a small mismatch between the natural morphology of the diblock and the substrate pattern is permissible if defect-free registration and order is required. Using blends of AB -diblock copolymers with the corresponding A- and B-homopolymers is an experimentally convenient way to adjust (enlarge) the domain spacing and it also is crucial for replicating more complex patterns. This is illustrated in Fig. 12 where the ordering of a ternary blend on a nested array of bends is shown. The periodicity of the stripes matches the bulk lamellar spacing but the distance between the AB interfaces at the corners is larger. The homopolymers redistribute as to selectively swell the morphology at the corners resulting in defect free ordering. Note also the Ω -shape of the AB -interface at the corners which resembles domain shapes observed at grain boundaries in the bulk.[59]

If one increases the mismatch between the length scale or the symmetry of the substrate pattern and the bulk morphology of the diblock the copolymers do no longer register with the substrate pattern. This is illustrated in Fig. 13 which shows the disordered bicontinuous morphology of a lamellar-forming ternary blend on top of a surface pattern that consist of a square array of spots with center-to-center distance, $\lambda = 1.21L_0$, and radii, $R = 0.30L_0$.

Near the substrate the morphology replicates the substrate pattern and forms a quadratically perforated lamellar (QPL) sheet [28]. Necks of polystyrene (PS) connect to this QPL. The near-

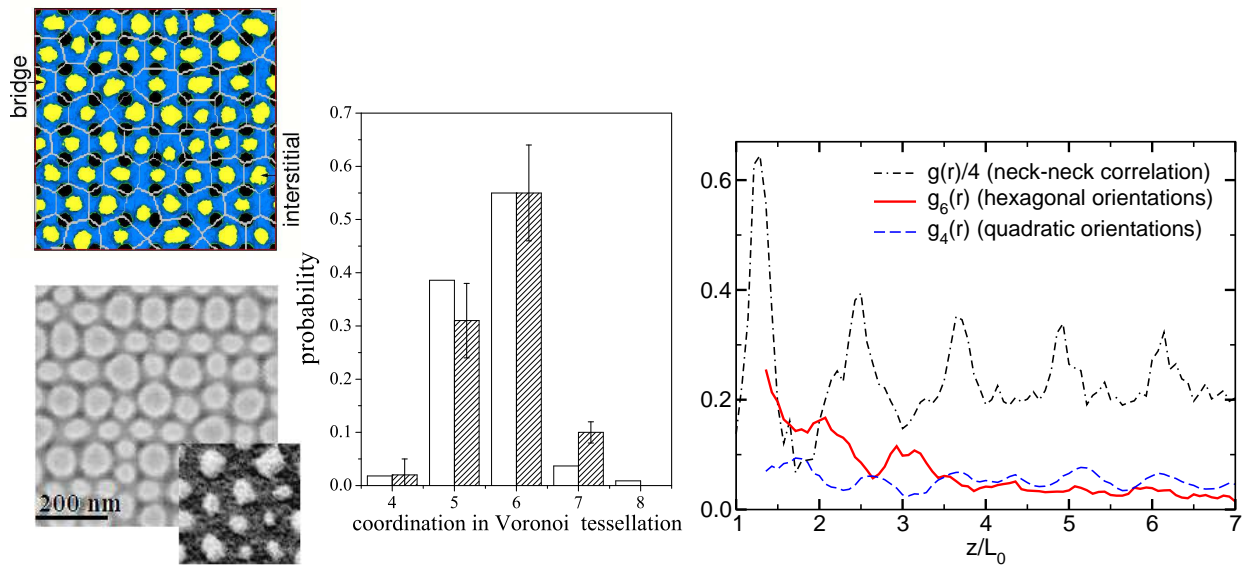


Fig. 13: Morphology of a copolymer/homopolymer blend film of thickness $D_0 = 0.63L_0$ and lateral dimensions of $9.77L_0$ on a square array of spots. (top left) SCMF simulation showing only the top view of the PS-rich domains (white/yellow) and the interface between PS and PMMA (dark grey/blue). Regions on top of the spots are PMMA-rich (transparent) and one looks through to the substrate (black). The position between two PMMA-attracting spots of the substrate is denoted as “bridge”, while the position at the center of a plaquette of four spots is denoted “interstitial”. The Voronoi tessellation of the necks is indicated by thin white lines. (bottom left) SEM image of the composition at the film surface. The PS-domains are shown in light grey while PMMA-rich surface areas correspond to dark grey regions. Note that the PS-domains appear artificially larger in the SEM images so a more accurate view of the domain sizes is provided by an AFM phase image shown as an inset at the lower right corner. (middle) Probability distribution of the coordination (number of edges) of Voronoi cells (c.f. top left panel). The “errorbars” of experimental data (shown in grey) characterize the variance of results obtained by analyzing different SEM images of size $9.77L_0$. SCMF simulation results are shown as open bars. (right) Pair correlation of the necks and orientational correlation functions for hexagonal and square orientations extracted from large SEM images. From Ref. [28]

substrate morphology favors a square geometry of the necks while the packing of dense necks rather results in a hexagonal structure. This competition prevents the formation of long-range order and one observed in the SCMF simulations as well as in the experiments a disordered bicontinuous structure. The local geometry can be characterized by a Voronoi tessellation which reveals a substantial amount of 6-fold coordinated necks. The local hexagonal structure is also revealed by the orientational correlation function, g_6 [61].

$$g_n(r) = \left\langle \left| \frac{1}{n} \sum_{\alpha \in \langle \text{nn} \rangle_i} e^{in\phi_{\alpha i}} \frac{1}{n} \sum_{\beta \in \langle \text{nn} \rangle_j} e^{-in\phi_{\beta j}} \right| \right\rangle \quad (48)$$

where α and β run over all nearest neighbors (nn) (as identified via the neck-neck-pair correlation function) of the two necks i and j a distance r apart and $\phi_{\alpha i}$ is the angle of the vector between the center of the neck i and its neighbor α . Hexagonal correlations are strong but short-ranged while orientational correlations with $n = 4$ are weaker but longer-ranged and are mediated over long distances by the substrate pattern.

3 Outlook

The computational techniques – simulations, SCF theory, and SCMF simulations – provide a wealth of information about the structure and thermodynamics of polymer systems. The examples illustrate applications on length scales comparable or larger than the molecular size in the framework of coarse-grained models. Only minimal coarse-grained models have been utilized that focus on the relevant long wave length properties in order to access large length- and time scales. The computational techniques can readily be applied to models that retain details of the chemical architecture and thus mimic the behavior of a specific systems. Much effort has been devoted to systematically construct coarse-grained models that strike a balance between computational efficiency and description of chemical details. The combination of efficient computational techniques and coarse-grained model will remain crucial for studying this important and fascinating class of materials.

References

- [1] R. W. Cahn, P. Haasen and E. J. Kramer, *Materials Science and Technology, A Comprehensive Treatment*, Vol 12, VCH, Weinheim (1993); F. Garbassi, M. Morra and E. Occhiello, *Polymer Surface: From Physics to Technology*, Wiley, Chichester (2000).
- [2] P. J. Flory, J. Chem. Phys. **9**, 660 (1941); H. L. Huggins, J. Chem. Phys. **9**, 440 (1941).
- [3] I. Carmesin and K. Kremer, Macromolecules **21**, 2819 (1988); H.-P. Deutsch and K. Binder, J.Chem.Phys. **94**, 2294 (1991).
- [4] M. Müller, Macromol. Theory Simul. **8**, 343 (1999).
- [5] K. Kremer and G.S. Grest, J. Chem. Phys. **92**, 5057 (1990).
- [6] C. Bennemann, W. Paul, K. Binder, and B. Dünweg, Phys. Rev. E **57**, 843 (1998).
- [7] M. Müller and L.G. MacDowell, Macromolecules **33**, 3902 (2000).
- [8] F. Wang and D. P. Landau, Phys. Rev. Lett. **86**, 2050 (2001).
- [9] F. Schmid and M. Müller, Macromolecules **28**, 8639 (1995).
- [10] B.A. Berg and T. Neuhaus, Phys. Rev. Lett. **68**, 9 (1992); B.A. Berg, Comp. Phys. Comm **153**, 397 (2003).
- [11] A. Sariban and K. Binder, Macromolecules **21**, 711 (1988); **24**, 587 (1991); J. Chem. Phys. **86**, 5859 (1987); Makromol. Chem. **189**, 2357 (1988).
- [12] C. Borgs and R. Kotecky, J. Stat. Phys. **60**, 79 (1990); Phys. Rev. Lett. **68**, 1734 (1992).
- [13] M. Müller and K. Binder, Macromolecules **28**, 1825 (1995).
- [14] K. Binder, Phys. Rev. A **25**, 1699 (1982).
- [15] M. Müller, K. Binder, and W. Oed, J. Chem. Soc. Faraday Trans. **91**, 2369 (1995).
- [16] P. Virnau and M. Müller, J. Chem. Phys. **120**, 10925 (2004).
- [17] J. Valleau, Adv. Chem. Phys. **105**, 369 (1999).
- [18] E. Helfand, Y. Tagami, J. Polym. Sci. **B 9**, 741 (1971); J. Chem. Phys. **56**, 3592 (1971); **57**, 1812 (1972); E. Helfand, A. M. Sapse, J. Chem. Phys. **62**, 1327 (1975); E. Helfand, J. Chem. Phys. **62**, 999 (1975).
- [19] J. Noolandi and K.M. Hong, Macromolecules **14**, 727 (1981).
- [20] K.R. Shull, Macromolecules **26**, 2346 (1993).
- [21] J.M.H.M. Scheutjens, G.J. Fleer, J. Phys. Chem. **83**, 1619 (1979); *ibid* **84**, 178 (1979); Macromolecules **18**, 1882 (1985).
- [22] M.W. Matsen and M. Schick, Phys. Rev. Lett. **74**, 4225 (1995).

- [23] G.H. Fredrickson, V. Ganesan, and F. Drolet, *Macromolecules* **35**, 16 (2002).
- [24] M. Müller and F. Schmid, *Adv. Polym. Sci.* **185**, 1 (2005).
- [25] A. C. Shi, J. Noolandi, and R. C. Desai, *Macromolecules* **29**, 6487 (1996).
- [26] E. Reister, M. Müller and K. Binder, *Phys. Rev. E* **64**, 041804 (2001).
- [27] M. Müller and G.D. Grant, *J. Polym. Sci. B* **43**, 934 (2005).
- [28] K.Ch. Daoulas, M. Müller, M.P. Stoykovich, S.-M. Park, Y.J. Papakonstantopoulos, J.J. de Pablo, and P.F. Nealey, *Phys. Rev. Lett.* (in print).
- [29] S. F. Edwards, *Proc. Phys. Soc.* **85**, 613 (1965).
- [30] M. Müller, *Monte Carlo Simulations of Binary Polymer Liquids*, in *Molecular Simulation Methods for Predicting Polymer Properties*, V. Galiatsatos (ed), Wiley Hoboken, NJ (2005).
- [31] F.S. Bates, M.F. Schultz, J.H. Rosedale, and K. Almdal, *Macromolecules* **25**, 5547 (1992); M.D. Gehlsen and F.S. Bates, *Macromolecules* **27**, 3611 (1994); F.S. Bates and G.H. Fredrickson, *Macromolecules* **27**, 1065 (1994).
- [32] D. Schwahn, G. Meier, K. Mortensen, and S. Janssen, *J.de.Phys. II (France)* **4**, 837 (1994); H. Frielinghaus, D. Schwahn, L. Willner, and T. Springer, *Physica B* **241**, 1022 (1998).
- [33] K. Binder, *J. Chem. Phys.* **79**, 6387 (1983).
- [34] F. P. Buff, R. A. Lovett and F. H. Stillinger, *Phys. Rev. Lett.* **15**, 621 (1965).
- [35] W. Helfrich, *Z. Naturforsch.* **28c**, 693 (1973).
- [36] J.D. Weeks, *J. Chem. Phys.* **67**, 3106 (1977).
- [37] D. Bedeaux and J.D. Weeks, *J. Chem. Phys.* **92**, 972 (1985).
- [38] A.N. Semenov, *J. Phys. (France) II* **6**, 1757 (1996).
- [39] A. Werner, F. Schmid, M. Müller, K. Binder, *J. Chem. Phys.* **107**, 8175 (1997).
- [40] A. Werner, F. Schmid, M. Müller, K. Binder, *Phys. Rev. E* **59**, 728 (1999).
- [41] M. Müller und A. Werner, *J. Chem. Phys.* **107**, 10764 (1997).
- [42] M. Müller und M. Schick, *J. Chem. Phys.* **105**, 8885 (1996).
- [43] A.N. Semenov, *Macromolecules* **26**, 6617 (1993).
- [44] M.D. Lacasse, G.S. Grest, and A.J. Levine, *Phys. Rev. Lett.* **80**, 309 (1998).
- [45] M. Müller, E. V. Albano, and K. Binder, *Phys. Rev. E* **62**, 5281 (2000).
- [46] K. R. Shull, A. M. Mayes, and T. P. Russell, *Macromolecules* **26**, 3929 (1993).
- [47] T. Kerle, J. Klein, and K. Binder, *Phys. Rev. Lett.* **77**, 1318 (1996).

- [48] M. Sferrazza, C. Xiao, R.A.L. Jones, D.G. Bucknall, J. Webster, and J. Penfold, *Phys. Rev. Lett.* **78**, 3693 (1997).
- [49] L. Leibler, *Macromolecules* **13**, 1602 (1980).
- [50] A.N. Semenov, *Soviet Physics JETP* **61**, 733 (1985).
- [51] G. H. Fredrickson and E. Helfand, *J. Chem. Phys.* **87**, 697 (1987).
- [52] G.J. Kellogg, D.G. Walton, A.M. Mayes, P.Lambooy, T.P. Russell, P.D. Gallagher, and S.K. Satija, *Phys.Rev.Lett.* **76**, 2503 (1996).
- [53] D.G. Walton, G.J. Kellogg, A.M. Mayes, P. Lambooy, and T.P Russell, *Macromolecules* **27**, 6225 (1994).
- [54] G.T. Pickett and A.C. Balazs, *Macromolecules* **30**, 3097 (1997).
- [55] M.W. Matsen, *J.Chem.Phys.* **106**, 7781 (1997).
- [56] T. Geisinger, M. Müller, and K. Binder, *J. Chem. Phys.* **111**, 5241 (1999).
- [57] T. Geisinger, M. Müller, and K. Binder, *J. Chem. Phys.* **111**, 5251 (1999).
- [58] E.W. Edwards, M.P. Stoykovich, M. Müller, H.H. Solak, J.J. de Pablo and P.F. Nealey, *J. Polym. Sci. B* **43**, 3444 (2005).
- [59] M.P. Stoykovich, M. Müller, S.O. Kim, H.H. Solak, E.W. Edwards, J.J. de Pablo, and P.F. Nealey, *Science* **308**, 1442 (2005).
- [60] N. Rehse, A. Knoll, M. Konrad, R. Magerle, and G. Krausch, *Phys. Rev. Lett.* **87**, 035505 (2001).
- [61] D.R. Nelson and B.I. Halperin, *Phys. Rev. B* **19**, 2457 (1979).